Computational efficiency of frequency- and time-domain calculations of extreme mass-ratio binaries: Equatorial orbits

Jonathan L. Barton,[1] David J. Lazar,[1] Daniel J. Kennefick,[2] Gaurav Khanna,[3] and Lior M. Burko[1,4]

[1]*Department of Physics, University of Alabama in Huntsville, Huntsville, Alabama 35899, USA*
[2]*Department of Physics, University of Arkansas, Fayetteville, Arkansas 72701, USA*
[3]*University of Massachusetts at Dartmouth, North Dartmouth, Massachusetts 02747, USA*
[4]*Center for Space Plasma and Aeronomic Research, University of Alabama in Huntsville, Huntsville, Alabama 35899, USA*

(Received 7 April 2008; published 15 September 2008)

Gravitational waveforms and fluxes from extreme mass-ratio inspirals can be computed using time-domain methods with accuracy that is fast approaching that of frequency-domain methods. We study in detail the computational efficiency of these methods for equatorial orbits of fast spinning Kerr black holes, and find the number of modes needed in either method—as functions of the orbital parameters—in order to achieve a desired accuracy level. We then estimate the total computation time and argue that for high-eccentricity orbits the time-domain approach may be more efficient computationally. We suggest that in practice low-m modes are computed using the frequency-domain approach, and high-m modes are computed using the time-domain approach, where m is the azimuthal mode number.

DOI: 10.1103/PhysRevD.78.064042 PACS numbers: 04.25.Nx, 04.30.Db, 04.30.−w

I. INTRODUCTION AND SUMMARY

Compact stellar mass objects emit gravitational waves in the good-sensitivity band of the planned Laser Interferometer Space Antenna (LISA) during their last year of inspiral into a supermassive black hole. The gravitational waveforms of extreme mass-ratio inspirals (EMRIs) are therefore of interest and when observed may shed light on the spacetime of the central black hole, including testing the Kerr hypothesis [1], in addition to being a sensitive tool to measure the central black hole's parameters. This possibility makes such sources of gravitational waves extremely interesting, despite the relatively low number of sources expected during the lifetime of the LISA mission. Specifically, tens to hundreds of such sources are expected to redshifts of $z \sim 0.5$–1 [2]. In addition, the solution of the two body problem in general relativity remains challenging, and EMRIs orbits and waveforms correspond to its solution in the extreme mass-ratio limit.

EMRIs in the good-sensitivity frequency band for LISA are expected to span a wide range in eccentricity. Specifically, such sources are believed to be created as a result of the compact object's scattering by multibody interactions onto a possibly highly eccentric orbit in the spacetime of the central black hole. For central black holes with mass of $M = 3 \times 10^6 M_\odot$, it was shown by Hopman and Alexander [3] that the probability distribution function of compact objects entering the LISA band has support for eccentricity ϵ in the range $0 \lesssim \epsilon \lesssim 0.81$ which peaks for $\epsilon \sim 0.6$–0.7. Intermediate mass black holes would have even higher eccentricities. Specifically, it was shown in [3] that for a central black hole of mass $M = 10^3 M_\odot$, the maximal eccentricity is $\epsilon_{\max} = 0.998$ and all inspiraling compact objects (except for white dwarfs that are likely to be tidally torn) are likely to have eccentricities close to the maximal value. The wide range of eccentricities of possible EMRI sources for LISA raises the question of how the construction of theoretical templates depends on the parameters of the EMRI. Specifically, we are interested in how different approaches to compute theoretical gravitational-wave templates depend on the eccentricity.

Construction of theoretical templates is important both for detection of EMRIs gravitational waves and for accurate parameter estimation. Numerical waveforms can be constructed using the frequency-domain (FD) or the time-domain (TD) approaches. The former approach has been developed to very high accuracy and is considered robust and accurate [4–7]. On the other hand, advances to the TD approach have been hindered first by the success of the FD approach [7,8], and by the crudity of the initial attempts to evolve numerically the fields coupled to a pointlike source with the Teukolsky equation [9,10]. Significant improvement in the accuracy of TD solutions of the inhomogeneous Teukolsky equation, i.e., the 2 + 1D solution of the Teukolsky equation coupled to a point mass, was recently achieved in [11,12]. For the first time, it was shown that TD calculations can be as accurate as FD calculations. The TD method of [11] was improved with the introduction of the ''discrete delta'' model of the source [12] and an appropriate low pass filter that makes the discrete delta useful also for eccentric or inclined orbits [13]. Specifically, correlation integrals of gravitational waveforms done for the same system in the FD and TD approaches show that the two agree to a high level [13]. One may therefore argue that the two methods are comparable in the results they are capable of producing. We therefore contend that the viewpoint that the TD solution of the inhomogeneous Teukolsky equations is far from being competitive from the FD solution can no longer be supported. However, we believe that one should not seek competition of the two

approaches, but rather how they complement each other, as either method has nonoverlapping strengths. In order to achieve this goal one needs to compare the computational efficiency of the two approaches. In this paper we arbitrarily set the accuracy level in practice at the level of 10^{-3} for comparison (except for Table I that does not require such an accuracy level.) However, there is no fundamental limit to the accuracy level in either the FD or the TD approaches. Progress in the computational method may both improve accuracy levels and reduce computational time. The set accuracy level introduces an error in the energy and angular momentum fluxes and in the gravitational waveforms that is then translated as errors in the estimation of the system's parameters. This error in parameter estimation is common to either computational method when the waveforms are computed to the same accuracy level. This paper discusses codes that at the time this work was starting were the state of the art of either approach. We believe that this paper still captures the main features of the approaches discussed in general and are not particular to the specific codes used.

The question of the efficiency and the computation time with which the results are obtained remains an open question though. The common wisdom is that the FD computation is more effective computationally than its TD counterpart: FD approaches are particularly convenient when the system—and the emitted gravitational waves—exhibits a discrete set of frequencies. Indeed, as shown by Schmidt [14] and by Drasco and Hughes [15], all bound Kerr orbits have a simple, discrete spectrum of orbital frequencies. However, generic orbits and, in particular, high-eccentricity orbits, although in principle amenable to a Fourier decomposition and a FD construction of the waveforms, require the summation of many terms in the Fourier series. This problem limits the accuracy and increases the computation time in FD calculations. While this statement, or similar ones, appear in the literature [8], it has not been quantified.

The motivation of this paper is to study the relative computational efficiency of FD and TD codes for the solution of the inhomogeneous Teukolsky equation. Specifically, we study the question of how much computational time is needed to find the fluxes of energy and angular momentum to infinity from an eccentric and equatorial orbit around a fast spinning Kerr black hole. We restrict the analysis here to equatorial orbits. The analysis of equatorial orbits is nontrivial and teaches much of the method and properties also of nonequatorial orbits. The analysis of nonequatorial orbits increases considerably the volume of the parameter space, and we leave its study to the future. We do, nevertheless, comment on the analysis of generic orbits.

The estimation of the total needed computation time for TD codes is relatively simple: after the desired accuracy level is set, one needs to estimate the number of azimuthal m modes (associated with the ϕ orbital angular frequency) required for the total sum over m modes to achieve the desired accuracy, and then compute each m mode at the same accuracy level. The number of needed m modes is not hard to estimate, because the partial fluxes approach a geometric progression in m for large m values, with the asymptotic factor between two successive partial fluxes depending on the eccentricity of the orbit. After the needed number of m modes is determined, one can use the TD code of [11] (possibly with the improvements included in [12,13]) to calculate the partial fluxes and sum over them. Using the asymptotic geometric progression structure one may also estimate the error associated with the summation

TABLE I. Average (over one period) fluxes per unit mass extracted at $r = 100M$ for a central black hole with $a/M = 0.9$, and a prograde eccentric orbit of semilatus rectum $p = 4.64M$, for various values of the eccentricity ϵ. For each mode m, we show in bold print the mode that corresponds to the eccentricity for which the highest flux is achieved. Notice that the data presented in this table are rather coarse and are only intended to demonstrate the overall behavior. The accuracy level of data in this Table is at the 5%–10% level. Fine details are studied below.

$\lvert m\rvert$	$\epsilon = 0.1$	0.5	0.7	0.8	0.9
1	1.03×10^{-6}	$\mathbf{1.32\times10^{-6}}$	1.19×10^{-6}	1.07×10^{-6}	1.05×10^{-6}
2	6.96×10^{-4}	$\mathbf{8.73\times10^{-4}}$	7.84×10^{-4}	6.49×10^{-4}	3.32×10^{-4}
3	1.50×10^{-4}	2.57×10^{-4}	$\mathbf{2.68\times10^{-4}}$	2.37×10^{-4}	1.30×10^{-4}
4	4.12×10^{-5}	9.34×10^{-5}	$\mathbf{1.10\times10^{-4}}$	1.03×10^{-4}	5.86×10^{-5}
5	1.16×10^{-5}	3.59×10^{-5}	$\mathbf{4.92\times10^{-5}}$	4.61×10^{-5}	2.86×10^{-5}
6	3.58×10^{-6}	1.50×10^{-5}	$\mathbf{2.31\times10^{-5}}$	2.28×10^{-5}	1.48×10^{-5}
7	1.06×10^{-6}	6.48×10^{-6}	1.12×10^{-5}	$\mathbf{1.16\times10^{-5}}$	7.80×10^{-6}
8	3.25×10^{-7}	2.83×10^{-6}	5.56×10^{-6}	$\mathbf{6.07\times10^{-6}}$	4.28×10^{-6}
9		1.27×10^{-6}	2.79×10^{-6}	$\mathbf{3.21\times10^{-6}}$	2.37×10^{-6}
10		5.72×10^{-7}	1.42×10^{-6}	$\mathbf{1.72\times10^{-6}}$	1.33×10^{-6}
11		2.65×10^{-7}	7.30×10^{-7}	$\mathbf{9.31\times10^{-7}}$	7.53×10^{-7}
12		1.25×10^{-7}	3.63×10^{-7}	$\mathbf{5.05\times10^{-7}}$	4.19×10^{-7}
13		5.50×10^{-8}	1.94×10^{-7}	$\mathbf{2.76\times10^{-7}}$	2.39×10^{-7}

over the partial fluxes and verify that the desired accuracy level is indeed achieved. This is done in Sec. II. The TD calculation of the individual partial fluxes can be done more efficiently than a straightforward calculation of the fields to very late times and great distances that are required for an accurate estimate of the fluxes at infinity. Specifically, one can make use of the peeling properties of the Weyl scalars at great distances and fit the fields at finite distances to that behavior. One may then use the fitted behavior to extract the behavior at infinity. This is done in the Appendix. We find this method to be cleaner and better motivated physically than the fit done in [12] that uses a general two-parameter fit function of a form which is not strongly motivated physically.

The estimation of the total needed computation time for FD codes starts similarly to the TD analysis: specifically, one needs to first determine the number of m modes needed for the determined accuracy level. This can be done in a similar way to how it is done in the TD. The calculation of each m mode in the FD approach requires the summation over a number of k, n, and ℓ modes that correspond to the radial and angular (about the equatorial plane) orbital angular frequencies and the radiative multipole ℓ. Because we focus attention on equatorial plane orbits, the n, ℓ modes trivialize, and in practice only the k modes are of importance. We find in Sec. III that the number of k modes that one needs to sum over to achieve the desired accuracy level increases with the eccentricity and with the corresponding value of m in an intricate manner.

Next, in Sec. IV we estimate the computation time of each k mode, and find it is a function of k. The behavior of the computation time of the k mode is found to have a rather intricate dependence of the value of k. We use this behavior to approximate the computation time over a sum of k modes up to some $k_{\max}$, and argue it is approximately quadratic in $k_{\max}$ for high $k_{\max}$ values. Then, in Sec. V we find the total computation time for all the FD modes on the same machine on which we perform the TD computation, and compare the two. We find that the FD code is more efficient at low m values (for a twofold reason: because those require few k modes, and for low m values each k mode takes less time to compute), but the computation time increases rapidly with the value of m. We find the growth rate of the computation time with the mode number m to increase as a power of m, with the value of the exponent increasing with the eccentricity. Finally, we estimate that for generic orbits the two methods become comparable already for moderately high values of the eccentricity, in the range of $\epsilon \sim 0.6$–0.7 or higher. Higher eccentricity orbits are more efficiently calculated using the TD approach. Even when the calculation of the sum of all m modes is done more efficiently using one method over the other, one may still compute the low m modes using the FD approach and the high m modes using the TD approach. Such a hybrid method may prove to be the most efficient computationally. One should also consider the fact that the total needed number of k modes is an empirically found number. When the full parameter space is mapped, one may tabulate the numbers of required modes as functions of the orbital parameters. Until this is done, extra computation time is needed to find the number of needed modes, including the computation of some modes that are found *a posteriori* to be unneeded. No similar problem occurs in the TD approach.

II. SUMMING OVER THE m MODES

To obtain the sum over all m modes we need to obtain results for high m numbers and find a way to determine (i) how many m modes we need to sum over to get the total flux to a certain predetermined accuracy, and (ii) estimate the error in neglecting all the higher m modes. In the case of circular and equatorial orbits, Finn and Thorne [6] show that (see [6] for more details and for definitions)

$$\dot{E}_m = \frac{2(m+1)(m+2)(2m+1)!m^{2m+1}}{(m-1)[2^m m!(2m+1)!!]^2}\eta^2\tilde{\Omega}^{2+2m/3}\dot{\mathcal{E}}_{\infty m}$$

which has the nice property that $\dot{E}_{m+1}/\dot{E}_m \to$ const as $m \to \infty$. (Note that this property depends on the factor of $\tilde{\Omega}^{2+2m/3}$.) We may therefore approximate the sum over infinitely many modes by taking the series to be a geometric progression.

For eccentric orbits we no longer have the Finn-Thorne formula, but we can do numerical experiments to test whether the same results hold also for such orbits. We first show in Table I the average fluxes obtain for a number of eccentric orbits (with a fixed value of the semilatus rectum p) as a function of the mode m. The data presented in Table I are intentionally coarse and are not intended to be more accurate than at the 5%–10% level. Below, we also present similar data with higher accuracy, where the latter are needed. We plot in Fig. 1 $\dot{E}_m$ as a function of m for several eccentric orbits. We see that for all values of ϵ, the dropoff rate is exponential in m for large values of m. The highest partial flux is in the fundamental mode, $m = 2$, and is highest for $\epsilon \sim 0.5$. This result is indeed expected: The radiated power in gravitational waves averaged over one period for a point mass μ in a Keplerian orbit around a Schwarzschild black hole of mass M is given by the quadrupole formula to be [16]

$$\langle P\rangle = \frac{32}{5}\frac{\mu^2M^2(M+\mu)}{a^5(1-\epsilon^2)^{7/2}}\left(1+\frac{73}{24}\epsilon^2+\frac{37}{96}\epsilon^4\right).$$

Recalling that the semimajor axis a is related to the semilatus rectum p by $p = a(1-\epsilon^2)$, we find that for fixed p,

$$\langle P\rangle \sim (1-\epsilon^2)^{3/2}\left(1+\frac{73}{24}\epsilon^2+\frac{37}{96}\epsilon^4\right),$$

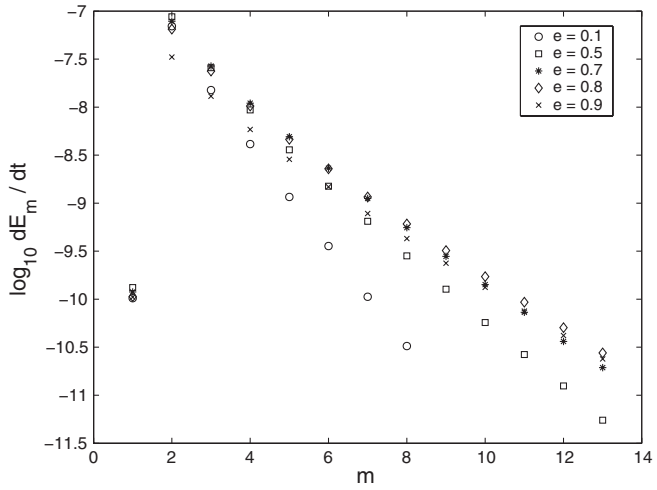

FIG. 1. The flux in the m mode as a function of m for various values of the eccentricity e. The black hole's spin is $a/M = 0.9$ and the orbit's semilatus rectum is $p/M = 4.64$.

which has a maximum at $\epsilon = 0.465$. As the partial flux in any other mode is suppressed by over an order of magnitude compared with the fundamental mode ($m = 2$), this result for the total flux is carried over to the fundamental mode. The larger m, we find numerically that the larger the eccentricity for which most flux is obtained.

We next consider the ratio of the relative contribution of the m mode to the partial-sum (up to m) flux compared with the preceding mode, as a function of m. An asymptotic dropoff of the flux corresponds to this ratio approaching a constant value as $m \to \infty$. In Fig. 2 we plot this ratio as a function of m for various values of the eccentricity.

Last, we extrapolate the curves in Fig. 2 to find the asymptotic value for the ratio and plot it in Fig. 3 as a

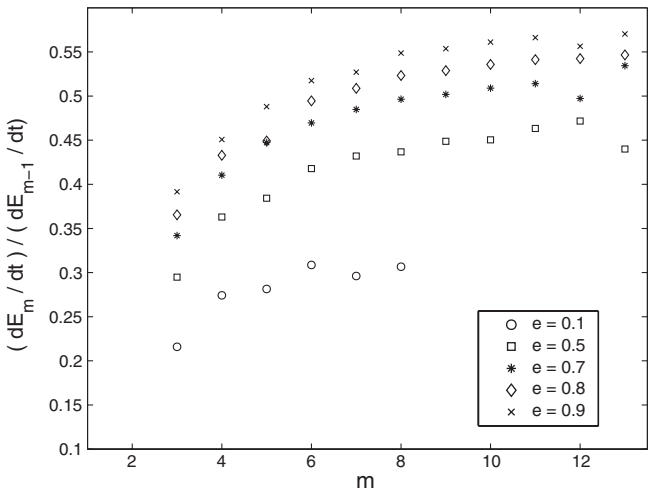

FIG. 2. The ratio of the relative contribution of the m mode to the partial-sum (up to m) flux compared with the preceding mode, as a function of m, for various values of the eccentricity e. Same parameters as in Fig. 1.

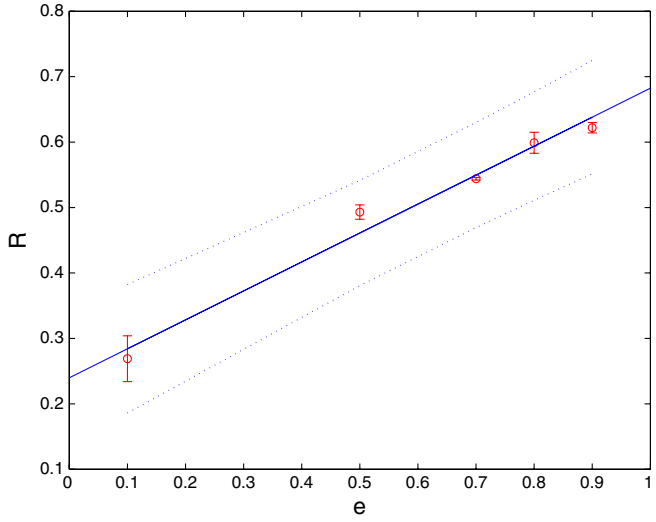

FIG. 3 (color online). The asymptotic ratio R as a function of the eccentricity e. The individual error bars are shown, in addition to the best-fit curve (solid line) and 3σ confidence curves (dotted lines).

function of the eccentricity ϵ. The best-fit curve is given by $R = 0.24 + 0.44\epsilon$ with a correlation coefficient $R^2 = 0.980438$.

As $\dot{E}_m$ behaves asymptotically similar to a geometric progression, we can approximately sum over all modes (provided sufficiently many modes are calculated, so that the sequence of partial fluxes already converges approximately to the asymptotic behavior). Specifically, calculating the sequence $\dot{E}_1, \dot{E}_2, \dot{E}_3, \ldots, \dot{E}_{n-1}, \dot{E}_n$, we can calculate the partial sums $S_n := \sum_{m=1}^{n} \dot{E}_m$, and the remainder is approximated by $R_n \sim \dot{E}_n R/(1 - R)$, where R is the

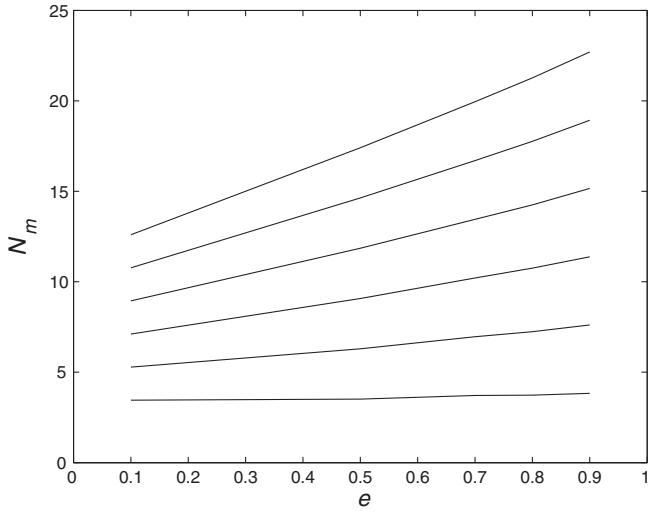

FIG. 4. The number of m modes necessary for the sum over m modes to have a certain accuracy. We plot contour curves at a fixed level of accuracy, showing the number of m modes needed as a function of the eccentricity e. The contours are at accuracy levels of 10^{-1}, 10^{-2}, 10^{-3}, 10^{-4}, 10^{-5}, and 10^{-6}.

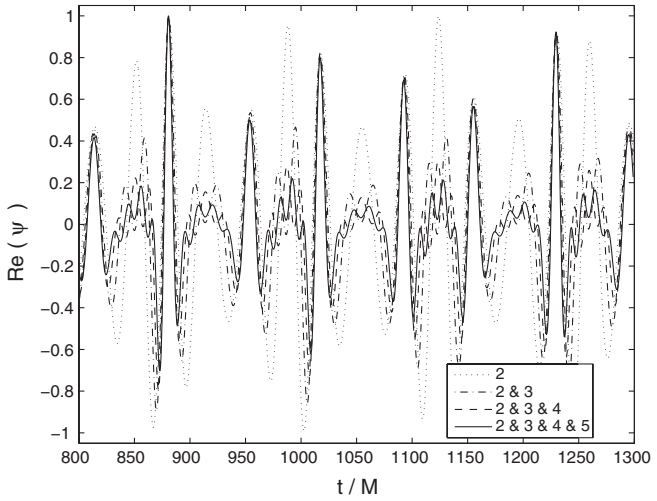

FIG. 5. The real part of the waveform on the equatorial plane at $r/M = 625$ for $a/M = 0.9$, $p/M = 4.64$, and $\epsilon = 0.1$ for $\psi_{m=2}$ (dotted line), $\psi_2 + \psi_3$ (dash-dotted line), $\psi_2 + \psi_3 + \psi_4$ (dashed line), and $\psi_2 + \psi_3 + \psi_4 + \psi_5$ (solid line) as a function of t/M.

asymptotic ratio evaluated above. One can then approximate the total flux by $\dot{E}_{\rm Total} \sim S_n + R_n$ and use $\Delta_n = R_n/\dot{E}_{\rm Total}$ as a measure for the error. We can therefore answer questions such as "how many modes m do we need to sum over to obtain a desired accuracy level?" (assuming each mode individually has the desired accuracy level). We show this in Fig. 4 that shows contour curves at a fixed accuracy level on the number of m-modes-eccentricity plane.

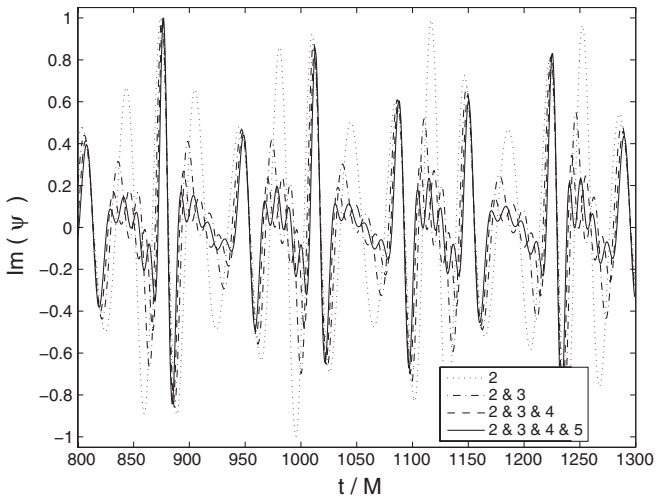

FIG. 6. The imaginary part of the waveform on the equatorial plane at $r/M = 625$ for $a/M = 0.9$, $p/M = 4.64$, and $\epsilon = 0.1$ for $\psi_{m=2}$ (dotted line), $\psi_2 + \psi_3$ (dash-dotted line), $\psi_2 + \psi_3 + \psi_4$ (dashed line), and $\psi_2 + \psi_3 + \psi_4 + \psi_5$ (solid line) as a function of t/M.

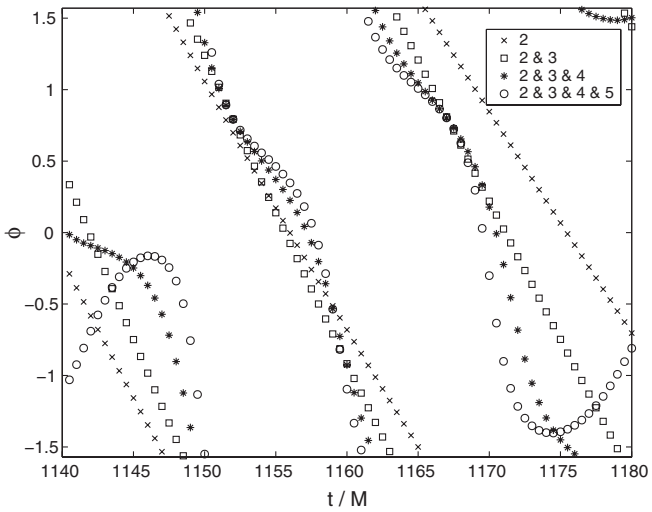

FIG. 7. The phase of the waveform on the equatorial plane for the same parameters as in Fig. 5. Shown are the phases corresponding to $\psi_{m=2}$ ($\times$), $\psi_2 + \psi_3$ ($\square$), $\psi_2 + \psi_3 + \psi_4$ (*), and $\psi_2 + \psi_3 + \psi_4 + \psi_5$ ($\bigcirc$), as a function of t/M.

Based on Fig. 4, to determine the energy flux to 10% accuracy requires 4 modes at all values of the eccentricity ϵ. We may therefore find the approximate total waveform by summing over the 4 modes of greatest energy flux. For $a/M = 0.9$, $p/M = 4.64$, and $\epsilon = 0.1$, we show in Figs. 5 and 6 the waveform obtained when summing over these 4 modes, specifically $m = 2, 3, 4, 5$. Indeed, the phase information is captured well by the sum of these 4 modes and is no longer changing significantly by the addition of more modes, as is shown in Fig. 7.

III. SUMMATION OVER MULTIPOLES ℓ AND k MODES

The behavior of the m modes—that corresponds to the angular frequency Ω_ϕ—is common to both time-domain and frequency-domain approaches. In the TD case, however, the study of the behavior of the m modes summarizes all the modes that need to be considered to get the full waveform and the total fluxes radiated. In the FD case, however, one needs to consider also the modes that arise from the three different frequencies of the problem: the k modes, corresponding to the radial angular frequency Ω_r, and the n modes, corresponding to the inclination angle oscillations with angular frequency Ω_θ. (We note that various authors exchange the notation of the latter two frequencies, $k \leftrightarrow n$.) Here, we concentrate on the equatorial plane and defer discussion on motion outside the equatorial plane to a sequel.

The FD code that we use is based on the code presented in [8], where more details on the code can be found in addition to descriptions of the tests done to check the code and the sources for errors. The FD numerical method is based on that of [5] and solves the Sasaki-Nakamura

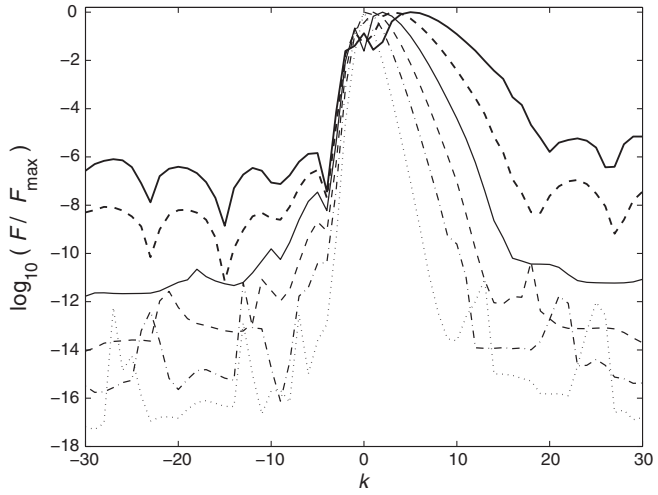

FIG. 8. The flux in different k modes, after summation over all ℓ, for $m = 2$, for $a/M = 0.9$ and $p/M = 4.64$: $\epsilon = 0.1$ (dotted line), $\epsilon = 0.2$ (dash-dotted line), $\epsilon = 0.3$ (thin dashed line), $\epsilon = 0.4$ (thin solid line), $\epsilon = 0.5$ (thick dashed line), and $\epsilon = 0.6$ (thick solid line). For each value of the eccentricity, the flux is normalized to the flux at the value of k for which the flux is maximal.

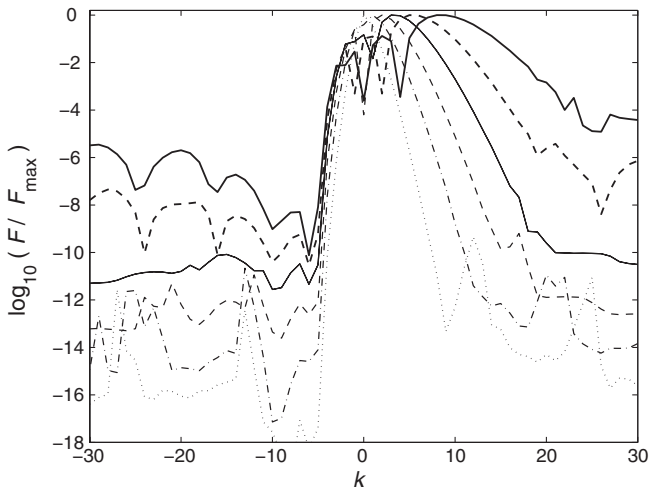

FIG. 9. Same as Fig. 8 for $m = 3$.

equation [17] using the Burlisch-Stoer integration. The accuracy level of the code is at the level of 10^{-6}–10^{-4}.[1]

The first indication to the increase in the number of necessary k modes with increasing eccentricity was shown in [10]. It should be noticed, however, that the results presented in [10] for $\epsilon = 0.8$ may be more indication of the failure of the solution of the radial Teukolsky equation in the frequency domain and the need for the Sasaki-Nakamura formulation thereof than a true behavior of the k modes. Figure 8 shows the flux in each k mode for $m = 2$, after all ℓ modes were summed over for $a/M = 0.9$ and $p/M = 4.64$ for different values of the eccentricity. Similar figures were obtained also for other values of m. Figures 8 and 9 suggest the following types of behavior: first, the value of k for which the flux is maximal shifts to higher values with the increase in eccentricity of the orbit. Second, with increasing eccentricity, the flux curve broadens (mostly for positive values of k, so that the curve becomes less and less symmetric in k for high ϵ). We also find (Fig. 10) that the peaks of the flux curves become m modal, i.e., at high values of ϵ the flux curve breaks into a number of peaks equal to the mode m. Similar behavior was reported first in [8]. The peaks' backgrounds exhibit interesting oscillations that appear to be independent (or, at the most, weakly dependent) of m and ϵ. The broadening of the flux curves suggests that more k modes are required in order to obtain the total flux. In what follows we quantify this statement and make it precise.

[1]Recently, possible inaccuracies for very large k values were noticed. These inaccuracies occur for larger values of k than those used here and therefore do not affect our results.

The number of k modes required at a fixed value of the eccentricity ϵ to obtain the total flux to a desired accuracy increases logarithmically with the accuracy. This behavior is described in Fig. 11 that plots the error involved in the inclusion of the N_k modes (of the greatest partial fluxes) as a function of N_k for various values of the eccentricity ϵ. In all cases this behavior is exponential. Notice, however, that the slope of the fitted curve becomes steeper with increasing eccentricity. This behavior suggests that as the eccentricity increases, the rate at which the number of k modes that are required in order to obtain the same level of accuracy increases. This rate also increases with the mode number m (Fig. 12). Notice, from Fig. 10, that also the number of *negative* k modes increases with the mode number m (for fixed eccentricity), although not as fast as the number of positive k modes. In Fig. 13 we show the

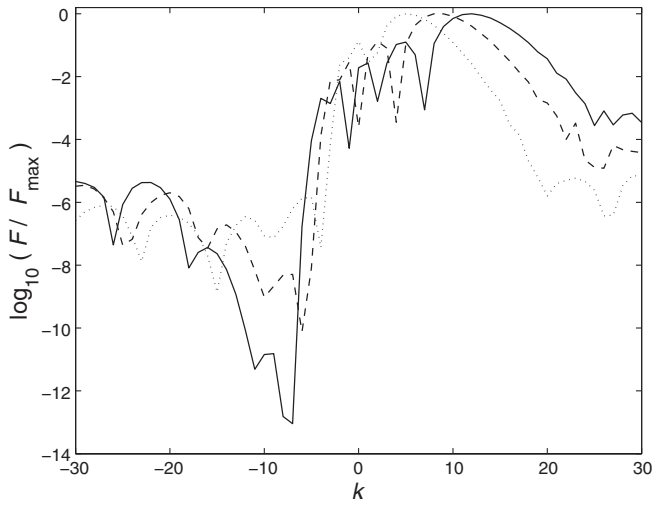

FIG. 10. Same as Fig. 8, for $m = 2$ (dotted line), $m = 3$ (dashed line), and $m = 4$ (solid line), for $\epsilon = 0.6$. Notice that the first two curves repeat data already presented in Figs. 8 and 9.

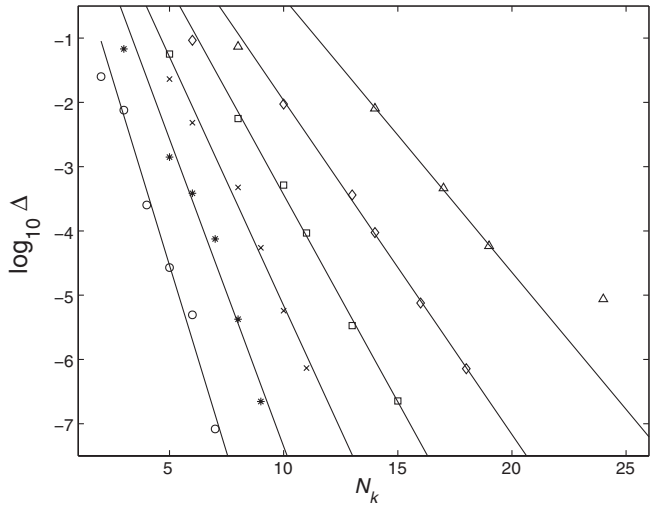

FIG. 11. The error Δ in summing over a number N_k of k modes, after summation over all ℓ, for $m = 2$, for $a/M = 0.9$ and $p/M = 4.64$: $\epsilon = 0.1$ (○), $\epsilon = 0.2$ (*), $\epsilon = 0.3$ (×), $\epsilon = 0.4$ (□), $\epsilon = 0.5$ (◇), and $\epsilon = 0.6$ (△). For each value of the eccentricity, the solid line describes a fitted line as follows: corresponding to increasing eccentricity: $\log_{10}\Delta = 1.2796 - 1.1630N_k (R^2 = 0.9810)$, $\log_{10}\Delta = 2.2131 - 0.9567N_k$ ($R^2 = 0.9691$), $\log_{10}\Delta = 2.5781 - 0.7740N_k$ ($R^2 = 0.9774$), $\log_{10}\Delta = 3.0085 - 0.6445N_k$ ($R^2 = 0.9962$), $\log_{10}\Delta = 3.2273 - 0.5197N_k$ ($R^2 = 0.9987$), $\log_{10}\Delta = 3.8898 - 0.4267N_k$ ($R^2 = 0.9383$). For each fitted curve we include the square of the correlation coefficient R^2.

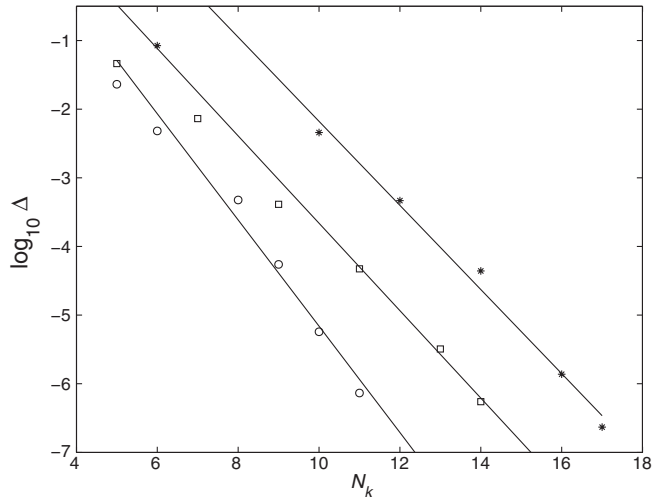

FIG. 12. The error Δ in summing over a number N_k of k modes, after summation over all ℓ, for $a/M = 0.9$, $p/M = 4.64$, and $\epsilon = 0.3$: $m = 2$ (○), $m = 3$ (□), and $m = 4$ (*). For each value of the eccentricity, the solid line describes a fitted line as follows, corresponding to increasing value of m: $\log_{10}\Delta = 2.5781 - 0.7740N_k$ ($R^2 = 0.9774$), $\log_{10}\Delta = 2.7038 - 0.6366N_k$ ($R^2 = 0.9950$), $\log_{10}\Delta = 3.9493 - 0.6126N_k$ ($R^2 = 0.9893$). For each fitted curve we include the square of the correlation coefficient R^2.

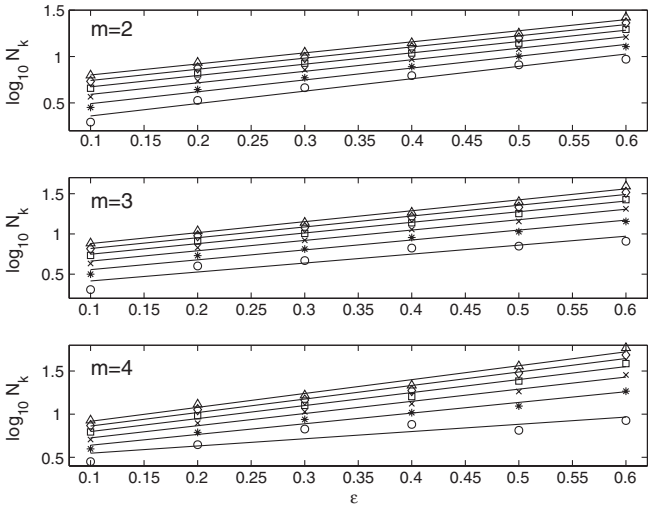

FIG. 13. The number N_k of k modes required for a given accuracy as a function of the eccentricity ϵ. Shown are 6 levels of accuracy and their corresponding contours: 10^{-1} (○), 10^{-2} (*), 10^{-3} (×), 10^{-4} (□), 10^{-5} (◇), and 10^{-6} (△), for three values of the mode number $m = 2$, 3, and 4. Upper panel ($m = 2$): the solid lines describe a fitted line as follows, corresponding the increasing accuracy: $\log_{10}N_k = 0.2253 + 1.3355\epsilon$ ($R^2 = 0.9642$), $\log_{10}N_k = 0.3632 + 1.2783\epsilon$ ($R^2 = 0.9872$), $\log_{10}N_k = 0.4671 + 1.2442\epsilon$ ($R^2 = 0.9945$), $\log_{10}N_k = 0.5506 + 1.2215\epsilon$ ($R^2 = 0.9959$), $\log_{10}N_k = 0.6206 + 1.2053\epsilon$ ($R^2 = 0.9948$), $\log_{10}N_k = 0.6808 + 1.1930\epsilon$ ($R^2 = 0.9928$). Middle panel ($m = 3$): the solid lines describe a fitted line as follows, corresponding the increasing accuracy: $\log_{10}N_k = 0.3040 + 1.1118\epsilon$ ($R^2 = 0.8860$), $\log_{10}N_k = 0.4321 + 1.2321\epsilon$ ($R^2 = 0.9727$), $\log_{10}N_k = 0.5329 + 1.2886\epsilon$ ($R^2 = 0.9900$), $\log_{10}N_k = 0.6151 + 1.3216\epsilon$ ($R^2 = 0.9934$), $\log_{10}N_k = 0.6844 + 1.3433\epsilon$ ($R^2 = 0.9932$), $\log_{10}N_k = 0.7442 + 1.1588\epsilon$ ($R^2 = 0.9919$). Lower panel ($m = 4$): the solid lines describe a fitted line as follows, corresponding the increasing accuracy: $\log_{10}N_k = 0.4636 + 0.8385\epsilon$ ($R^2 = 0.7739$), $\log_{10}N_k = 0.5159 + 1.2410\epsilon$ ($R^2 = 0.9747$), $\log_{10}N_k = 0.5841 + 1.4111\epsilon$ ($R^2 = 0.9894$), $\log_{10}N_k = 0.6478 + 1.5066\epsilon$ ($R^2 = 0.9884$), $\log_{10}N_k = 0.7050 + 1.5681\epsilon$ ($R^2 = 0.9853$), $\log_{10}N_k = 0.7564 + 1.6111\epsilon$ ($R^2 = 0.9821$).

number N_k of k modes required for a given accuracy as a function of the eccentricity ϵ, for different values of the mode number m. The increase in N_k is exponential in the eccentricity ϵ. For a given accuracy level, the exponential increase with ϵ becomes steeper as the mode number m increases, as shown in Fig. 14.

IV. MODES COMPUTATION TIME

The computation time of a single k mode is a function of k. To make a prediction of the k dependence of the computation time for a k mode we first write the radial Teukolsky equation

$$\Delta^2 \frac{d}{dr}\left(\Delta^{-1}\frac{dR_{\ell m\omega}}{dr}\right) - V(r)R_{\ell m\omega}(r) = -\mathcal{T}_{\ell m\omega}(r), \quad (1)$$

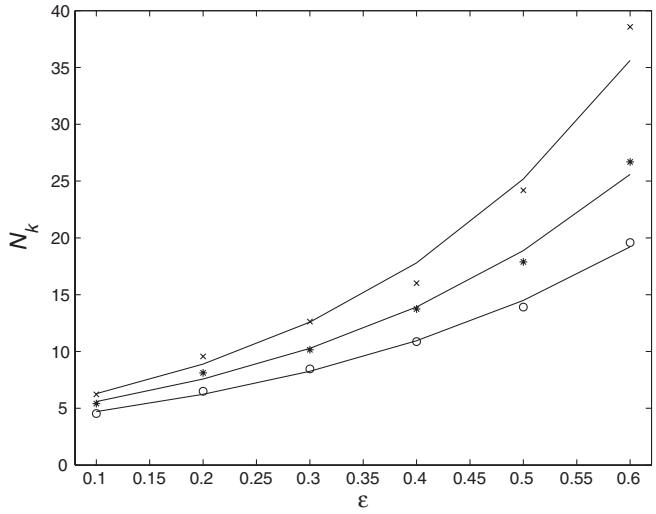

FIG. 14. The number N_k of k modes required for an accuracy of 10^{-4} as a function of the eccentricity ϵ. Shown are 3 values of m, and their corresponding contours, based on a fit to an exponential: $m = 2$ (○), $m = 3$ (*), and $m = 4$ (×).

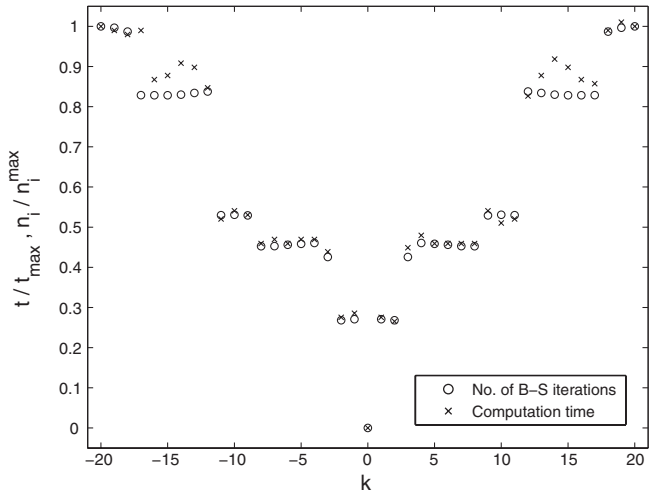

FIG. 15. The dependence of the computation time of a k mode on k: the computation time t (normalized by the maximal computation time is shown by ×, and the corresponding normalized number of iterations n_i that the Burlisch-Stoer engine does is shown in ○. The data are taken for $m = 0$, and for $p/M = 4.64$ and $\epsilon = 0.4$.

where the potential $V(r)$ is a complex valued function of r and the angular frequency ω [7]. The source term $\mathcal{T}_{\ell m\omega}(r)$ is a certain known function of the stress energy of the particle and its trajectory, and of the background geometry. As we are interested here only in the qualitative features of the solutions for Eq. (1), the details of the source are unimportant for us here. We next focus attention on the far field limit of Eq. (1). To gain a qualitative understanding of the structure of the solution, we next consider only the asymptotic solution as $r \to \infty$. In that limit, $R(r \to \infty) \sim r^3 e^{i\omega r_*}$ (corresponding to an outgoing solution), where r_* is the usual Kerr spacetime tortoise coordinate defined by $dr_*/dr = (r^2 + a^2)/\Delta$. The solution is an oscillatory solution in r with angular frequency ω. The typical length scale over which the solution is oscillating is therefore $\lambda \sim 2\pi/\omega$: the greater ω, the shorter the distance over which the solution oscillates.

The method we use to solve the frequency-domain equation is by a Burlisch-Stoer algorithm [18] that successively divides a single step into many substeps, until a (polynomial or rational) interpolation is accurate enough. If the original step happens to be too large (i.e., after a certain predetermined substep is calculated and the required accuracy is still not obtained), the original step will be bisected, and the process proceeds. Therefore, the greater ω and the shorter the oscillation length scale, the more divisions of the initial step are required, and the greater the number of substeps used to find the solution. As the angular frequency $\omega_{mk} = m\Omega_\varphi + k\Omega_r$, it is clear that the larger k (for a fixed value of m), the shorter the distance scale λ. We therefore expect the computation time of a single k mode to increase with k. In fact, the Burlisch-Stoer algorithm suggests that as ω_{mk} increases, the more substeps are needed, until for some value of k dividing the step into substeps is no longer sufficient, and the step is bisected. Then, division into substeps is again sufficient, until another k value is obtained for which the step is bisected. Each time the step is bisected, the total number of substeps computed jumps discontinuously, so that we expect the k-mode computation time to increase as a staircase function. In Fig. 15 we show the computation time of an individual k mode as a function of k, and also the number of Burlisch-Stoer iterations done. They both behave as expected. The preceding discussion suggests that a similar behavior of the computation time is found also as a function of m. This is indeed seen in Fig. 16.

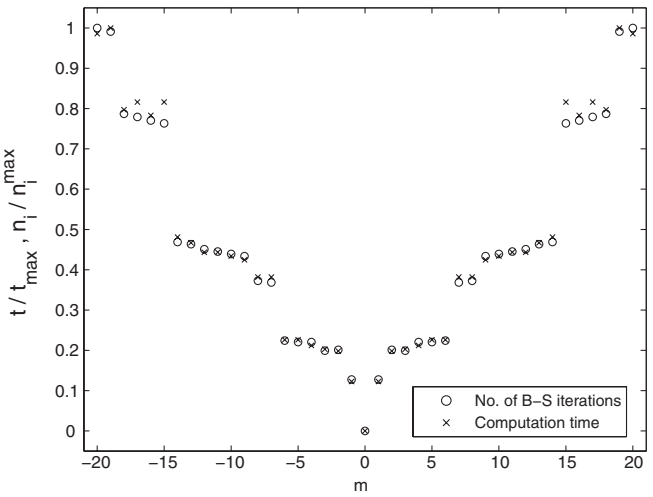

FIG. 16. Same as Fig. 15 for the m modes. Here, $k = 0$ and $\ell = 20$.

As can be seen from Figs. 15 and 16 the discontinuous jumps in the mode computation times occur at different values of m and k. Indeed, our discussion explains this behavior: jumps occur when the angular frequencies ω_{mk} arrive at some threshold values, corresponding to threshold wavelengths. As these threshold values should be about the same, we expect jumps to occur for m_j, k_j satisfying $k_j\Omega_r \sim m_j\Omega_\varphi$. Notice that $k_j(m_j)$ is defined here for vanishing $m(k)$. For the data presented here, for $\epsilon = 0.4$ we find $k_j/m_j \approx 1.33$, while $\Omega_\varphi/\Omega_r \approx 1.52$; for $\epsilon = 0.5$ we find $k_j/m_j \approx 1.40$, while $\Omega_\varphi/\Omega_r \approx 1.47$; and for $\epsilon = 0.6$ we find $k_j/m_j \approx 1.44$, while $\Omega_\varphi/\Omega_r \approx 1.39$, so that the difference between k_j/m_j and Ω_φ/Ω_r is at order 10%. We argue that these results support our interpretation of the discontinuous jumps in the computation time.

Our discussion suggests that for a fixed value of $k(m)$ and varying $m(k)$, there are values of the latter for which the computational time drops. These are the values that approximately satisfy $\omega_{mk} \lesssim \Omega_\varphi, \Omega_r$. (Recall that k and m can be either positive or negative.) That is, while fixing either k or m and varying the other, we expect to find a drop in the computation time (or, equivalently, in the number of Burlisch-Stoer iterations.) Indeed, we find this behavior as shown in Fig. 17. Notice, that for $k = 0$ the drop in computational time is found for $m = 0$, and as k increases, so does the value of m for which the drop is found. We also comment that this drop is broadened with increasing values of k.

The dependence of the computational time on the mode number k is therefore rather intricate. It can be approximated as follows: For each value of the eccentricity ϵ we take in practice the computational time of a single mode k to be a linear function of k that fits the computational data. This approximation underestimates the computation time

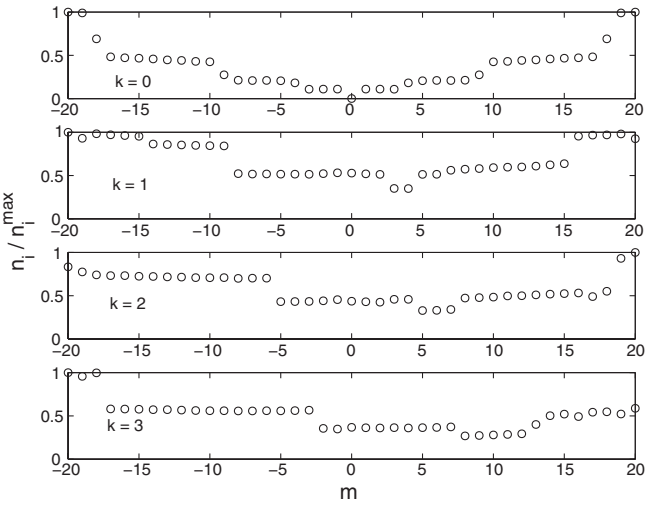

FIG. 17. Number of iterations of the Burlisch-Stoer solver as a function of m for fixed values of k, for the same orbital parameters as above, for $\epsilon = 0.1$.

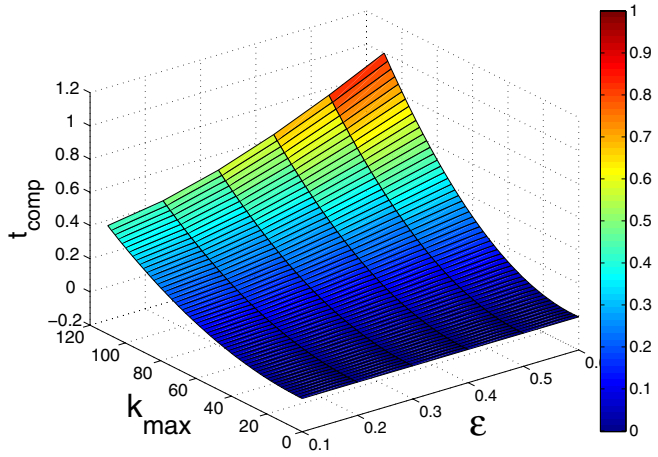

FIG. 18 (color online). The total computation time of the sum over k modes from $k = 0$ to $k = k_{\max}$ as a function of the eccentricity ϵ. The computation time is presented in units of the maximal computation time in the chosen range of parameters.

for some k modes, specifically those immediately following a discontinuous jump in the computation time, and overestimates the computation time for k modes just before a jump. However, as we are mostly interested in the total computation time of the sum over all modes, this approximation may be quite reasonable for the sum over all modes. In this approximation the sum over k modes up to some $k_{\max}$ is a quadratic function of $k_{\max}$. The total computation time of the sum of k modes from $k = 0$ to $k = k_{\max}$ as a function of the eccentricity is shown in Fig. 18. Notice that we can use Figs. 11 and 12 to find how many k modes we need to sum over to obtain the required accuracy level.

V. COMPARISON OF TOTAL COMPUTATION TIME OF TD AND FD CALCULATIONS

Finally, we put together all the previous results to compare the actual total calculation time of TD and FD codes. We choose an orbit that gives no special preference for one approach over the other, i.e., a moderate value for the eccentricity. In practice, we take $\epsilon = 0.5$ and $p = 4.64M$.

For the FD calculation we first set the desired level of accuracy, which in practice we choose here to be 10^{-3}, and then use Fig. 4 (or the data in Table I) to determine the number of m modes one needs to sum over to guarantee the desired accuracy level. The needed number of m modes is found in practice to be 7, for $m = 2, 3, \ldots, 9$.

For each individual m mode we then determine the number of k modes necessary to obtain the desired accuracy level. This determination is done with data as in Figs. 13 and 14. The values of the k modes we used in practice are as follows: for $m = 2$ we used $-2 \le k \le 10$, for $m = 3$ we used $-3 \le k \le 13$, for $m = 4$ we used $-3 \le k \le 16$, for $m = 5$ we used $-2 \le k \le 21$, for $m = 6$ we used $-1 \le k \le 23$, for $m = 7$ we used $-2 \le k \le 25$, for $m = 8$ we used $-1 \le k \le 28$, and for $m = 9$ we

TABLE II. Number of k modes for each m mode in the FD calculation, and the corresponding computation time in both the FD and TD calculations. The orbital parameters are $\epsilon = 0.5$, $p/M = 4.64$, and $a/M = 0.9$.

m mode	Range of k modes	Total k modes	FD time (s)	TD time (s)
2	$-2 \le k \le 10$	13	51	954
3	$-3 \le k \le 13$	17	99	945
4	$-3 \le k \le 16$	20	116	952
5	$-2 \le k \le 21$	24	179	942
6	$-1 \le k \le 23$	25	218	953
7	$-2 \le k \le 25$	28	254	953
8	$-1 \le k \le 28$	30	303	952
9	$-1 \le k \le 33$	35	391	942

used $-1 \le k \le 33$. Notice that the k modes we compute in each case are the full set of integers in a certain interval. That is, we do not seek out explicitly only the k modes that contribute significantly to the fluxes. This is done intentionally, as in practice one would sum over a stretch of k values: were one to seek out only the k values that contribute the most, one would have to calculate all k values anyway, in order to know which k modes are unimportant, so that the total computation time would remain the same. In all cases we computed $2 \le \ell \le 5$. The data are summarized in Table II and in Fig. 19. The FD calculations were optimized for the most efficient calculation for the desired accuracy level. Improvements to the computation time can be achieved, but only at the level of the code, e.g., making the Burlisch-Stoer algorithm more efficient. We believe that while such improvements can be made, their effect would be moderate. In this sense, the FD curve in Fig. 19 represents a lower bound on the FD calculation time. Increasing the eccentricity of the orbit ϵ would result in the FD curve of Fig. 19 moving up in the figure (an increase in the calculation time of each m mode, because of an increasing number of the required number of k modes and an increase in the computation time of individual k modes) and also having a faster growth rate.

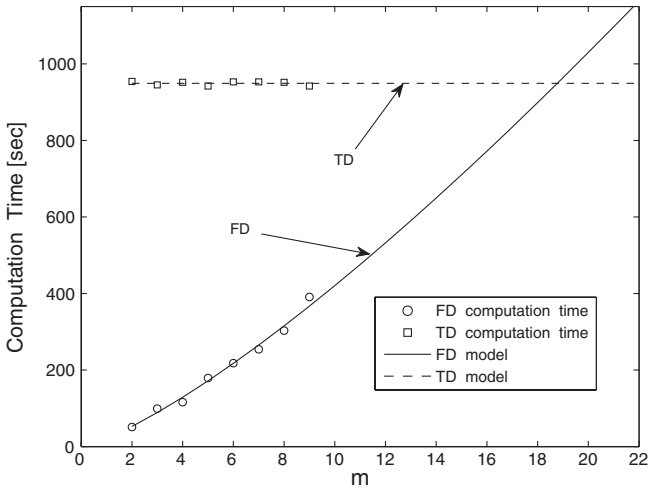

FIG. 19. Comparison of computation time for FD and TD for an orbit with $p/M = 4.64$ and $\epsilon = 0.5$ as a function of the mode number m. The circles (○) denote FD computation time, and the squares (□) show TD computation times. Both sets of runs were done on the same computer, in this case a single processor of a dual 2.7 GHz PowerPC G5. The curve is the fitted curve $t = 21.471 m^{1.2919}$ s, that fits the numerical data with a squared correlation coefficient of $R^2 = 0.9895$. For both cases the accuracy level is set at 10^{-3}.

For the TD calculations we used the 2 + 1D code of [11], with a radial resolution of $\Delta r = M/20$ (and a temporal resolution of $\Delta t = \Delta r/2$), and an angular resolution of $\Delta\theta = \pi/32$. We placed the inner and outer boundaries at $r_*/M = -50$ and at $r_*/M = 350$, respectively. We approximate the scattering problem on the boundaries by assuming Sommerfeld boundary conditions, i.e., no incoming radiation from outside the boundaries. One may of course make this approximation better by pushing the outer boundary outward (and the inner boundary inward). Reflections from the boundaries then do not contaminate the center of the computational domain (at $r_*/M = 150$) until $t/M = 400$, and we integrate in time until then. In practice, we wait at each evaluation point until the initial spurious waves (that result from imprecise initial data that correspond to a particle suddenly appearing at $t/M = 0$) have dispersed, and then average the flux over a full period of the orbit. The angular period is $T_\phi = 2\pi M^{-1/2}(r^{3/2} + aM^{1/2})$, where r is the semimajor axis. For our choice of parameters, $T_\phi \approx 102.4M$. The radial period is found to be $T_r \approx 162.5M$, and it is the latter (radial) period we use for our analysis. The fixed angular resolution level for all m modes slightly increases the TD computation time above what is necessary. Small m modes may be computed with cruder angular resolution, but for simplicity we did not change this parameter, so that in practice we have overestimated the TD computation time because of this parameter.

We extract the (radial period averaged) flux at a number of extraction distances, in practice at $r_*/M = 30, 40, \ldots, 100$, and then fit the (finite extraction distance) fluxes to an inverse-square function as in Eq. (A2). This allows us to achieve fluxes that agree with the FD fluxes to

10^{-3}, while not having to integrate to very late times (and commensurately increase also the spatial computational domain). Notably, we can obtain higher accuracy than that reported in [11] while integrating to a shorter time because we make use of the finite distance corrections to the energy flux. We discuss this method in detail in the Appendix.

The TD computational time is presented in Table II. It can be made more efficient using code improvements and data analysis improvements. First, we used Gaussian source modeling as in [11], and the discrete δ approach may improve efficiency considerably. In fact, Ref. [12] argued for a full order of magnitude reduction in computation time. While this statement may be an overestimate of the numerical capabilities—especially for generic (i.e., eccentric or inclined) orbits—it is certainly possible to improve the efficiency of the TD code by changing the method of calculation of the source term. (The discrete delta approach has also other advantages over the Gaussian model. See [12] for more detail.) If one were to obtain extremely high-accuracy results (using our current code with the Gaussian model for the pointlike source) we would have to do a series of complete simulations—with progressively narrower Gaussian profiles—and then take a numerical limit to represent a point source numerically. This procedure would additionally increase the TD computation time, perhaps even significantly. However, it is worth noting that using the discrete-delta model of [12] this is unnecessary, and the only convergence tests that remains are the ones based on standard grid resolution. Therefore, in a scenario of extremely high accuracy one may prefer to use that improved approach. Notice, nevertheless, that at our set level of accuracy the discussed procedure for the Gaussian model is not needed, and therefore the discrete-delta approach has no fundamental advantage. An important property of the TD code is that it is very naturally parallelizable. Certainly the FD computation is also parallelizable, most naturally by having each k mode computed on a different processor. In such a case, the total FD computation time is controlled by the k mode that takes the longest to compute, i.e., the largest k (see Fig. 15). Another improvement of efficiency of the FD code may come from improvements of the Burlisch-Stoer engine, specifically the solution for $\log r$ instead of r. It is currently unknown how the computational efficiency and numerical accuracy would be affected by such a change.

One factor that limits a possible reduction of the TD computation time is the need to average over an orbital (radial) period to find the average flux per period. Even for the strong field orbit considered here, with $p/M = 4.64$ and $\epsilon = 0.5$, the radial period is $T_r = 162.5M$, which puts a lower bound on how short the computational integration can be. One could perhaps shorten the computation time if only half an orbital period is computed, but because the phase of the orbit at the end of the spurious wave epoch is arbitrary, on the average at least three-quarters of an orbit need to be computed. However, we were interested here in comparison of the fluxes to infinity. If one is interested in the wave function itself, shorter computation times can be used, thus saving much of the TD computation time. No equivalent save in time can be achieved with the FD computation. Reduction of the TD computation time would result in the dashed line in Fig. 19 moving lower, thus making the computational time of TD and FD comparable already for lower m values.

It is important to emphasize that the comparison done here is limited to the energy and angular momentum fluxes. One may also be interested in the computation of the longest possible template for detection purposes, namely, a template as long as the dephasing time $t_{\rm dephase}$. As the dephasing time scales with $t_{\rm dephase} \sim \sqrt{M/\mu}$ [19], a longer computation time would be needed in the TD for extraction of the gravitational waveform for higher M/μ. A comparable increase in the computational time in the FD is not needed.

Most importantly, when higher eccentricity orbits are considered, the TD computation time remains unchanged, whereas the FD computation time increases considerably. More specifically, not only is the solid curve in Fig. 19 shifted up, it also becomes steeper (i.e., its rate of growth increases), so that the TD and FD computation times become comparable for lower m values. In addition, the TD calculation does not require any extra computation to find the waveform, as it is already available. In fact, an extra computation was needed to find the fluxes. On the other hand, the FD calculation requires an extra computation to produce the waveform, which we have not done here. Therefore, the greater efficiency of FD over TD for the modes shown here is much less impressive when the computation time for waveforms is of interest.

We therefore suggest that at high-eccentricity orbits the computational efficiency of the TD and the FD approaches is comparable for high m values. We believe that the question of the total (sum over m) computation time is not necessarily a very important one and suggest that for actual computations the low m modes are calculated using the FD approach, and the high m modes are calculated using the TD approach. The determination of which m values are low and which are high depends of course on the parameters of the system and the accuracy level of the computation. Using a single method, however, could still possibly make TD more efficient than FD for very high values of the eccentricity.

In the analysis of this paper we have focused on equatorial orbits. Such an orbit simplifies the problem, and not just computationally: the number of dimensions in the FD parameter space is significantly lower than that for generic orbits. While the analysis of equatorial orbits presented here is nontrivial, the added complications of handling generic orbits warrant separate treatment. When generic

orbits are considered, finding the number of ℓ modes required to achieve a set accuracy level with the FD approach becomes a nontrivial problem, as is the question of finding the computational time of each ℓ mode as a function of the mode number. Most importantly, the TD calculations remain unchanged, as does the associated computation time. We therefore expect the FD computation time to increase significantly with the transition from equatorial to inclined and then generic orbits, an increase that has no counterpart in the TD case. To do such an analysis, one needs to check the behavior of all combinations of the modes k, ℓ, and m, find the minimal number of modes required for a set accuracy level, and then compute those modes. The TD calculation requires that the same number of m modes are computed, and this computation time depends only on the duration of the computation, the size of the computational domain, and of course the grid resolution. Modest improvements to the TD computation time may be achieved by improving the efficiency of the source calculations (e.g., the discrete delta approach or alternative methods), but they are not expected to be as dramatic as previously suggested [12]. We expect the threshold eccentricity above which the TD approach is more computationally efficient than the FD approach for some of the needed m modes to be moderately high, possibly in the range of $\epsilon \sim 0.6$–0.7 or higher.

ACKNOWLEDGMENTS

The authors are indebted to Kostas Glampedakis for discussions and for making his FD code available to us, and to Steve Drasco for discussions. L. M. B. was supported in part by NASA/GSFC Grant No. NCC5-580, NASA/SSC Grant No. NNX07AL52A, by a minigrant from the Office of the Vice President for Research at UAHuntsville, and by NSF Grant No. PHY-0757344. G. K. is grateful for research support from the UMass Dartmouth COE, the HPC-Consortium, and Sony (SCEA). Many of the numerical computations presented in this paper were performed on a computer cluster built using *Playstation 3* gaming consoles [23], supplied by Sony R&D. D. J. L. was supported by Research Experiences for Undergraduates in Science and Engineering, sponsored by the Alabama Space Grant Consortium under Contract No. NNG05GE80H and by the UAHuntsville President's Office.

APPENDIX: NOTES ON WAVE-EXTRACTION DISTANCE FOR THE TIME-DOMAIN CODE

The peeling theorem describes how the various components of the gravitational field of a bound gravitational system behave as the observer moves away from the source (see, e.g., [20,21]). Specifically, in the wave zone of a radiating system, the Ψ_4 component of the Weyl curvature—which describes in the wave zone the outgoing transverse radiative degrees of freedom—typically drops off as $\Psi_4 \sim r^{-1}$, where r is the distance from the radiating system. The peeling theorem also gives the dropoff rates for the remaining Weyl scalars, and also for spin coefficients and other Newman-Penrose quantities. In addition to the leading order decay rate, the peeling theorem has been extended also to include correction terms in r^{-1}. Specifically, Newman and Unti showed that [22]

$$\Psi_4 = \frac{\Psi_4^0}{r} - \frac{2\alpha^0\Psi_3^0 + \bar{\xi}^{0k}\Psi_{3,k}^0}{r^2} + O(r^{-3}),$$

where α is a spin coefficient and ξ^i is an "integration constant" from the radial equations. A superscript 0 means the coefficient of the slowest decaying term in an expansion in r^{-1}. As the flux of energy in gravitational waves at infinity $\mathcal{F} \sim \lim_{r\to\infty} r^2\Psi_4^2 \sim (\Psi_4^0)^2$, Ψ_4^0 is directly related to the flux at infinity.

Notably, the leading order corrections in r^{-1} to Ψ_4 are proportional to the *asymptotic* value of the Weyl scalar Ψ_3 and its gradient. In the Teukolsky formalism, that conveniently describes black hole perturbations, the Weyl scalar $\Psi_3 \equiv 0$ ("transverse frame"), so that the leading order correction to Ψ_4 is at the next order: $\Psi_4 = \Psi_4^0/r + O(r^{-3})$. Therefore,

$$\mathcal{F} \sim \lim_{r\to\infty} r^2\Psi_4^2 \sim \lim_{r\to\infty} r^2\left[\frac{\Psi_4^0}{r} + O(r^{-3})\right]^2 \sim (\Psi_4^0)^2[1 + O(r^{-2})]. \tag{A1}$$

We therefore are motivated to introduce the ansatz

$$\dot{E} = \dot{E}_\infty[1 - A(m\lambda\!\!\!^{-}/r)^2], \tag{A2}$$

where $\lambda\!\!\!^{-} := \lambda/(2\pi) = (r_0^{3/2} + aM^{1/2})/(mM^{1/2})$, and r_0 is the Boyer-Lindquist radius of the orbit. Notice that $m\lambda\!\!\!^{-} = \Omega^{-1}$, so that our ansatz can be written as $\dot{E} = \dot{E}_\infty[1 - A(\Omega r)^{-2}]$. Note that the expansion parameter $(\Omega r)^{-2} \ll 1$, as the field is evaluated far from the radiating system, specifically outside the "light cylinder." This ansatz is also suggested by Fig. 1 of Ref. [11] and by Table VI of Ref. [12], where a best fit was done to the ansatz $\dot{E}_{\rm SKH} = \dot{E}_\infty[1 - q(r_0/r)^p]$, and the free parameter p was found numerically to be rather close to 2 (with deviations of $\lesssim 3\%$) for a large range of orbits.

We test our ansatz by fitting the outgoing flux of energy for a number of circular and equatorial orbits around a Kerr black hole as detected at a sequence of distances from the radiating system to the ansatz (A2). In Table III we show the outgoing fluxes from particles in circular orbits around a Kerr black hole, taken at a sequence of distances. Table IV shows the squared correlation coefficient for the various cases we have checked. In all cases the high value of the correlation coefficient corroborates our ansatz. In Table V we show the values of the free parameter A for the same cases. Lastly, in Table VI we compare the flux to infinity based on the ansatz (A2) to the flux obtained from a

TABLE III. Fluxes per unit mass extracted from the time-domain code at a sequence of radii on the numerical grid. $\dot{E}_R$ is the flux per unit mass measured at a radius RM. For $|m| = 2, 3$ the data are identical to Table V of Ref. [12]. Notice that in [12] (and also Tables I, II of [11]) each value of $|m|$ is in fact the sum of the contributions of m and $-m$.

$\|m\|$	r_0/M	a/M	$\dot{E}_{100}$	$\dot{E}_{200}$	$\dot{E}_{300}$	$\dot{E}_{400}$	$\dot{E}_{500}$	$\dot{E}_{600}$
1	4.0	0.99	1.2779×10^{-6}	1.3049×10^{-6}	1.3107×10^{-6}	1.3130×10^{-6}	1.3143×10^{-6}	1.3150×10^{-6}
2	4.0	0.99	1.2284×10^{-3}	1.2341×10^{-3}	1.2351×10^{-3}	1.2355×10^{-3}	1.2356×10^{-3}	1.2357×10^{-3}
3	4.0	0.99	2.9481×10^{-4}	2.9639×10^{-4}	2.9667×10^{-4}	2.9677×10^{-4}	2.9681×10^{-4}	2.9682×10^{-4}
4	4.0	0.99	8.3615×10^{-5}	8.4525×10^{-5}	8.4769×10^{-5}	8.4865×10^{-5}	8.4924×10^{-5}	8.4955×10^{-5}
5	4.0	0.99	2.6586×10^{-5}	2.6875×10^{-5}	2.6949×10^{-5}	2.6982×10^{-5}	2.7000×10^{-5}	2.7015×10^{-5}
1	10	0.90	1.9565×10^{-8}	2.4481×10^{-8}	2.5424×10^{-8}	2.5735×10^{-8}	2.5888×10^{-8}	2.5968×10^{-8}
2	10	0.90	2.0865×10^{-5}	2.1965×10^{-5}	2.2161×10^{-5}	2.2228×10^{-5}	2.2259×10^{-5}	2.2275×10^{-5}
3	10	0.90	2.3396×10^{-6}	2.4794×10^{-6}	2.5043×10^{-6}	2.5128×10^{-6}	2.5167×10^{-6}	2.5188×10^{-6}
4	10	0.90	3.2046×10^{-7}	3.4170×10^{-7}	3.4576×10^{-7}	3.4723×10^{-7}	3.4796×10^{-7}	3.4836×10^{-7}
5	10	0.90	4.8313×10^{-8}	5.1497×10^{-8}	5.2112×10^{-8}	5.2330×10^{-8}	5.2438×10^{-8}	5.2500×10^{-8}
1	10	0.99	1.6454×10^{-8}	2.0725×10^{-8}	2.1513×10^{-8}	2.1778×10^{-8}	2.1907×10^{-8}	2.1976×10^{-8}
2	10	0.99	2.0516×10^{-5}	2.1605×10^{-5}	2.1799×10^{-5}	2.1884×10^{-5}	2.1914×10^{-5}	2.1931×10^{-5}
3	10	0.99	2.2889×10^{-6}	2.4279×10^{-6}	2.4526×10^{-6}	2.4610×10^{-6}	2.4629×10^{-6}	2.4670×10^{-6}
4	10	0.99	3.1481×10^{-7}	3.3596×10^{-7}	3.3998×10^{-7}	3.4144×10^{-7}	3.4208×10^{-7}	3.4329×10^{-7}
5	10	0.99	4.7238×10^{-8}	5.0395×10^{-8}	5.1012×10^{-8}	5.1174×10^{-8}	5.1122×10^{-8}	5.1182×10^{-8}
1	12	0.0	1.9126×10^{-8}	2.8001×10^{-8}	2.9932×10^{-8}	3.0499×10^{-8}	3.0772×10^{-8}	3.0928×10^{-8}
2	12	0.0	0.9792×10^{-5}	1.0628×10^{-5}	1.0777×10^{-5}	1.0827×10^{-5}	1.0850×10^{-5}	1.0862×10^{-5}
3	12	0.0	0.9769×10^{-6}	1.0663×10^{-6}	1.0825×10^{-6}	1.0881×10^{-6}	1.0906×10^{-6}	1.0920×10^{-6}
4	12	0.0	1.1883×10^{-7}	1.3096×10^{-7}	1.3321×10^{-7}	1.3401×10^{-7}	1.3440×10^{-7}	1.3462×10^{-7}
5	12	0.0	1.5953×10^{-8}	1.7590×10^{-8}	1.7874×10^{-8}	1.7982×10^{-8}	1.8033×10^{-8}	1.8062×10^{-8}

TABLE IV. Correlation coefficient R^2 for the ansatz. The roman numerals list the four orbits considered. I: $r_0 = 4M$, $a = 0.99M$; II: $r_0 = 10M$, $a = 0.9M$; III: $r_0 = 10M$, $a = 0.99M$; IV: $r_0 = 12M$, $a = 0$. Notice we have changed the order of the orbits compared to the previous paper, to arrange them in ascending order of wavelengths. For all cases, the fit is done with 6 data points, at values of $r/M = 100$, 200, 300, 400, 500, and 600. (The case II-4 has a different extraction location.)

m mode	1	2	3	4	5
I	0.998 976 026	0.999 984 27	0.999 899 201	0.995 686 2	0.995 075 07
II	0.999 991 39	0.999 961 89	0.999 960 31	0.999 946 517	0.999 942 24
III	0.999 996 44	0.999 961 71	0.999 957 83	0.998 752 311	0.999 972 98
IV	0.999 787 69	0.999 947 00	0.999 978 73	0.999 993 86	0.999 975 05

TABLE V. Best-fit value for the parameter A. The roman numerals designate the same orbits as in Table III. The bracketed number denotes the uncertainty in the last figure.

m mode	1	2	3	4	5
I	3.5458(2)	0.757 53(2)	0.866 47(5)	1.9655(3)	1.9622(4)
II	2.3812(2)	0.615 6(4)	0.691 5(4)	0.7751(5)	0.7716(5)
III	2.4132(1)	0.622 4(4)	0.697 6(4)	0.799(2)	0.7734(5)
IV	2.250(2)	0.585 7(7)	0.628 7(5)	0.6950(3)	0.6917(5)

TABLE VI. Comparison of frequency-domain fluxes with time-domain fluxes extrapolated to infinity based on the ansatz (A2).

$\|m\|$	r_0/M	a/M	$\dot{E}_\infty$	$\dot{E}_{\rm FD}$	$(\dot{E}_\infty - \dot{E}_{\rm FD})/\dot{E}_{\rm FD}$
1	4.0	0.99	1.3153×10^{-6}	1.3403×10^{-6}	−0.0187
2	4.0	0.99	1.2359×10^{-3}	1.2418×10^{-3}	−0.0047
3	4.0	0.99	2.9689×10^{-4}	2.9621×10^{-4}	0.0023
4	4.0	0.99	8.4995×10^{-5}	8.6330×10^{-5}	−0.0155
5	4.0	0.99	2.7024×10^{-5}	2.7162×10^{-5}	−0.0051
1	10	0.90	2.6147×10^{-8}	2.6555×10^{-8}	−0.0154
2	10	0.90	2.2320×10^{-5}	2.2281×10^{-5}	0.0018
3	10	0.90	2.5245×10^{-6}	2.5221×10^{-6}	0.0010
4	10	0.90	3.4902×10^{-7}	3.5345×10^{-7}	−0.0125
5	10	0.90	5.2599×10^{-8}	5.3255×10^{-8}	−0.0123
1	10	0.99	2.2138×10^{-8}	2.2503×10^{-8}	−0.0162
2	10	0.99	2.1969×10^{-5}	2.1974×10^{-5}	−0.0002
3	10	0.99	2.4726×10^{-6}	2.4709×10^{-6}	0.0007
4	10	0.99	3.4388×10^{-7}	3.4467×10^{-7}	−0.0023
5	10	0.99	5.1469×10^{-8}	5.1687×10^{-8}	−0.0042
1	12	0.0	3.1227×10^{-8}	3.1456×10^{-8}	−0.0073
2	12	0.0	1.0897×10^{-5}	1.0861×10^{-5}	0.0033
3	12	0.0	1.0956×10^{-6}	1.0945×10^{-6}	0.0010
4	12	0.0	1.3503×10^{-7}	1.3658×10^{-7}	−0.0114
5	12	0.0	1.8121×10^{-8}	1.8317×10^{-8}	−0.0107

frequency-domain calculation. The associated errors appear to be larger for $m = 4, 5$ than for $m = 2, 3$. We attribute these higher errors to the lower values of the flux for high values of m. Specifically, to obtain the flux with the time domain one needs to first subtract the "flux" due to the spurious radiation associated with the initial time of the simulation [11]. As the fluxes become smaller, this subtraction becomes less accurate.

[1] J. R. Gair, C. Li, and I. Mandel, Phys. Rev. D **77**, 024035 (2008), and references cited therein.

[2] J. R. Gair, L. Barack, T. Creighton, C. Cutler, S. L. Larson, E. S. Phinney, and M. Vallisneri, Classical Quantum Gravity **21**, S1595 (2004).

[3] C. Hopman and T. Alexander, Astrophys. J. **629**, 362 (2005).

[4] M. Davis, R. Ruffini, W. H. Press, and R. H. Price, Phys. Rev. Lett. **27**, 1466 (1971); S. L. Detweiler, Astrophys. J. **225**, 687 (1978); E. Poisson, Phys. Rev. D **47**, 1497 (1993); **52**, 5719 (1995); **48**, 1860 (1993); T. Apostolatos, D. Kennefick, A. Ori, and E. Poisson, Phys. Rev. D **47**, 5376 (1993); E. Poisson and M. Sasaki, Phys. Rev. D **51**, 5753 (1995); C. Cutler, L. S. Finn, E. Poisson, and G. J. Sussman, Phys. Rev. D **47**, 1511 (1993); T. Tanaka, M. Shibata, M. Sasaki, and T. Nakamura, Prog. Theor. Phys. **90**, 65 (1993); M. Shibata, M. Sasaki, H. Tagoshi, and T. Tanaka, Phys. Rev. D **51**, 1646 (1995); T. Tanaka, Y. Mino, M. Sasaki, and M. Shibata, Phys. Rev. D **54**, 3762 (1996); S. Suzuki and K.-I. Maeda, Phys. Rev. D **58**, 023005 (1998); S. A. Hughes, Phys. Rev. D **64**, 064004 (2001); K. Glampedakis, S. A. Hughes, and D. Kennefick, Phys. Rev. D **66**, 064005 (2002).

[5] C. Cutler, L. S. Finn, E. Poisson, and G. J. Sussman, Phys. Rev. D **47**, 1511 (1993).

[6] L. S. Finn and K. S. Thorne, Phys. Rev. D **62**, 124021 (2000).

[7] S. A. Hughes, Phys. Rev. D **61**, 084004 (2000); **63**, 049902 (E) (2001).

[8] K. Glampedakis and D. Kennefick, Phys. Rev. D **66**, 044002 (2002).

[9] R. Lopez-Aleman, G. Khanna, and J. Pullin, Classical Quantum Gravity **20**, 3259 (2003).

[10] G. Khanna, Phys. Rev. D **69**, 024016 (2004).

[11] L. M. Burko and G. Khanna, Europhys. Lett. **78**, 60005 (2007).

[12] P. A. Sundararajan, G. Khanna, and S. A. Hughes, Phys. Rev. D **76**, 104005 (2007).

[13] P. A. Sundararajan, G. Khanna, S. A. Hughes, and S. Drasco, Phys. Rev. D **78**, 024022 (2008).

[14] W. Schmidt, Classical Quantum Gravity **19**, 2743 (2002).

[15] S. Drasco and S. A. Hughes, Phys. Rev. D **69**, 044015 (2004).

[16] P. C. Peters and J. Mathews, Phys. Rev. **131**, 435 (1963).

[17] M. Sasaki and T. Nakamura, Prog. Theor. Phys. **67**, 1788 (1982).

[18] W. H. Press, S. A. Teukolsky, W. T. Vetterling, and B. P. Flannery, *Numerical Recipes: The Art of Scientific Computing* (Cambridge University Press, Cambridge, 2007), 3rd ed..

[19] S. Drasco, Classical Quantum Gravity **23**, S769 (2006).

[20] H. Stephani, *Relativity: An Introduction to Special and General Relativity* (Cambridge University Press, Cambridge, England, 2004), 3rd ed.

[21] J. Stewart, *Advanced General Relativity* (Cambridge University Press, Cambridge, England, 1990).

[22] E. T. Newman and T. Unti, J. Math. Phys. (N.Y.) **3**, 891 (1962).

[23] http://gravity.phy.umassd.edu/ps3.html.